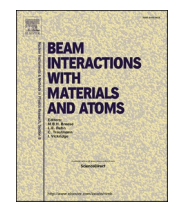
FISEVIER

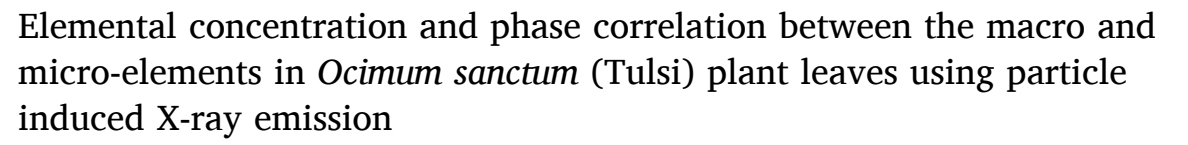
Contents lists available at ScienceDirect

Nuclear Inst. and Methods in Physics Research, B

journal homepage: www.elsevier.com/locate/nimb



Full Length Article





Darshpreet Kaur Saini, Todd A. Byers, Cory Nook, Charles T. Bowen, Mohin Sharma, Mritunjaya Parashar, Gary A. Glass, Bibhudutta Rout

Ion Beam Laboratory, Department of Physics, University of North Texas, Denton, TX 76203, USA

ARTICLE INFO

Keywords:
PIXE
Ocimum sanctum
X-ray spectroscopy
Elemental concentration
Tulsi

ABSTRACT

1. Introduction

Tulsi is known as the 'Queen of herbs' for its wide use in different health-related problems. It helps boost the metabolism of the system and is experimentally proven useful in antimicrobial, anti-hypersensitivity, and antioxidant activities [1]. Therefore, it has been a keen interest to study the presence of trace elements found in medicinal plants. Past studies have utilized techniques like total reflection X-ray fluorescence (TXRF) [2], and particle induced X-ray emission (PIXE) [3] to explore the elemental composition present in these plants, thus helping in better understanding of the effects of their intake in the human body [4].

When the high energy (MeV) ion beam is incident on the sample, the excitation of the inner shell electron of the target creates a vacancy that can be filled by non-radiative or radiative transitions. The non-radiative transitions include the transfer of the vacancy from one inner shell to another, and the difference of energy releases one of the outer shell electrons known as auger transition. The special case of auger emission is the Coster-Kronig transition in which the vacancy transfer occurs

within the same shell, from lower to higher subshell. The radiative transitions, PIXE for example, include the emission of outer shell electrons with the emission of characteristic X-rays. This study focuses on the X-ray spectrum analysis for the concentration of the elements present in the leaf sample and the correlation analysis based on the elemental maps generated from the scanning of the proton beam. Various techniques can generate elemental maps and study the elemental correlations, like scanning electron microscopy-energy dispersive X-ray spectroscopy (SEM-EDS) [5], secondary ion mass spectrometry (SIMS) [6], laser-induced breakdown spectroscopy (LIBS) [7], X-ray fluorescence spectroscopy (XRF), TXRF, and scanning transmission x-ray microscopy (STXM) [8]. However, SEM-EDS requires a flat and smooth sample surface for imaging and mapping. The interference from the bulk sample can affect the image contrast and causes the disappearance of fine structural features [5]. SIMS and LIBS are destructive techniques, whereas XRF provides semi-quantitative data at a lower image resolution [6,7]. TXRF and STXM have a limitation on the maximum thickness of a sample. The former requires thin amorphous

E-mail address: bibhu@unt.edu (B. Rout).

^{*} Corresponding author.

samples to reduce scattering effects, while the latter requires it to avoid the complete absorption of the incident light [8]. PIXE has advantages over the mentioned techniques as it provides higher sensitivity due to lower bremsstrahlung compared to electron microscopy, and better detection limits i.e., in ng/mg. Sample preparation is minimal as it can be performed on samples with inhomogeneous surfaces and different thicknesses.

The beam spot size was further reduced to the micron range (micro-PIXE) for high spatial resolution in the generated maps corresponding to the distribution of elements. To achieve a lateral resolution of ~ 1 um, the beam was focused using a set of quadrupoles magnetic focusing lenses in a separated quadruplet configuration [9]. As the beam scans over a selected area on the leaf, the detector registers the characteristic X-ray energies from each pixel along with position in x and y coordinates [10]. Then, all events are tagged to their x and y coordinates to generate a two-dimensional array of pixels, representing the elemental maps. PIXE has been used to find the elemental composition and their correlations [11], the spatial distribution of elements in various kinds of samples including biological and environmental samples like plant leaves [12,13,14,15], and hard human tissues [16]. It can also be used to analyze archeological samples like precious stones [17], pottery samples [18,19], and historical books [20]. Our study broadens the quantitative analysis from the elemental concentrations to elemental phase correlations in different regions of interest (ROI).

2. Sample preparation

Prior to analysis with a proton microbeam in vacuum, the leaf samples were washed with deionized water and shade-dried for a few days to preserve the nutritional level [21,22]. After that, 2 mm diameter leaf sections were removed using a circular punch. The samples were mounted on the sample holder and placed inside the microprobe chamber. On average, the leaf thickness was approximately 150 µm.

For broad-beam analysis, four leaf samples of Tulsi were dried with the help of a UV-lamp and covered with aluminum foil for 3–4 days. Afterward, they were ground into a fine powder using a mortar and pestle. The powdered samples were mixed with graphite powder to aid in conductivity for charge collection during ion beam analysis [23]. The powdered mixture was pressed into 6 mm diameter pellets with the help of a mechanical press. These pellets were mounted on a circular disc which was fitted onto the sample holder and transferred to the chamber for analysis.

3. Experimental methods and data collection

The samples were analyzed with a 2 MeV proton beam from 9SH Pelletron at the Ion Beam Laboratory (IBL) at the University of North Texas [24,25,26]. The probing beam spot size was $\sim 1~\mu\text{m}^2$ and the scanning area was of 375 \times 375 μm^2 for the micro-PIXE. The data was collected for 500 nC of incident charge with a beam current of 200 pA. For the broad-beam PIXE, an approximately 1 mm 2 beam spot size was used to collect the data for 1000 nC of the incident charge with a beam current of 700 pA.

The microprobe chamber comprises three detectors i.e., an X-ray detector for PIXE, a Passivated Implanted Planar Silicon (PIPS) charged particle detector for Rutherford backscattering spectrometry (RBS), and an additional PIPS detector for Scanning transmission ion microscopy (STIM), as shown in Fig. 1.

The X-ray detector is an Amptek X-123 Fast silicon drift detector [27] with a C1 window (light-tight window making it flexible enough to work in room light) and an area of 17.6 mm^2 and is mounted at 135° with respect to the ion beam direction. An 80-µm carbon filled polyethylene filter was mounted in front of the X-ray detector to protect it from the backscattered proton beam. A Faraday cup is mounted behind the target to collect the charge from thin samples. All the PIXE spectra and elemental maps were obtained using the acquisition system, OMDAQ-3 [28]. It processes the X-ray signal detected by the detector and converts it into a digital signal with the help of analog to digital converter (ADC). It provides a pulse height spectrum of the X-rays where the area under the peak contributes to the estimation of the concentration of the elements.

4. Data analysis

4.1. Utilizing micro-PIXE technique

The high-energy proton beam interaction also gives rise to the continuous background under the characteristic X-rays. The major contributor to the X-ray background is bremsstrahlung associated with the electrons ejected due to inelastic collisions. Additional overlaps with the PIXE spectrum also occur due to the escape peaks and detector pileup. Silicon escape peaks are produced due to the interaction of the elemental X-rays with the silicon crystal of the X-ray detector. When these X-rays escape from the detector, it results in a lower energy silicon peak than its actual value. Moreover, the pile-up phenomenon occurs when two incident X-rays arrive at the detector nearly simultaneously. In such instances, the electronic circuitry responsible for pulse detection may fail to discriminate between the two individual pulses, merging

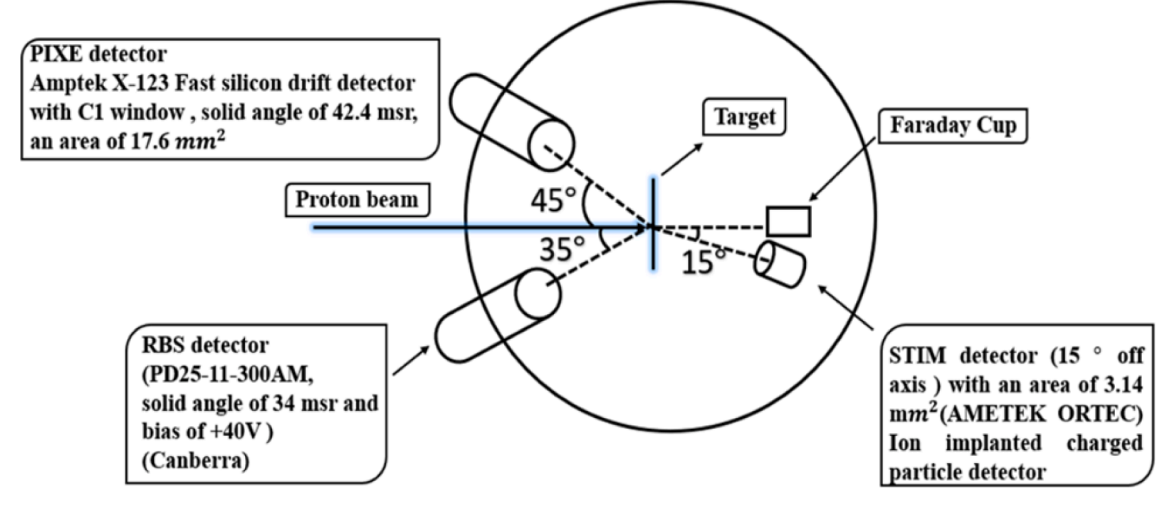


Fig. 1. Schematics of the Microprobe chamber, showing the position of the detectors, faraday cup, and target holder.

them into a singular pulse characterized by an energy equivalent to the summation of the energies of the constituent X-rays. The PIXE spectra were analyzed using GeoPIXE package [29] that extracts the peak information with the help of a Statistics-sensitive Non-linear Iterative Peak-clipping (SNIP) method that resolves all the overlapping of the X-ray peaks due to aforementioned reasons.

The elemental concentration maps were generated using the Dynamic analysis (DA) matrix method based on sample yield, information about the detector, its filter, and data acquisition dead time [30]. Each pixel in the map represents the product of concentration and the integrated charge giving the average concentrations of all the elements as the images are generated simultaneously with the incoming data from each scan [31]. The yield matrix contained the elements H, C, and O for the leaf base [32].

4.2. Utilizing broad-beam PIXE technique

Quantitative analysis of broad-beam PIXE spectra was also performed in GeoPIXE. The larger beam spot size provides the concentration of elements obtained over a larger region.

5. Results and discussion

5.1. Micro-PIXE

A micro-PIXE spectrum (red) along with bremsstrahlung background (blue), silicon escape peaks (magenta), and detector pileup (green) analyzed using GeoPIXE is shown in Fig. 2. For clarity, an expanded spectrum from 3 keV to 6 keV is shown in Fig. S1.

Metabolic processes primarily involve a limited number of elements, which are classified into two categories. The first category consists of macro-elements, essential nutrients found in higher concentrations, including H, C, N, O, P, S, K, and Ca. The second category comprises of micro-elements, which are found in trace amount, such as Cl, Mn, Fe, Cu, and Zn. The concentrations of macro-elements were 12633 ng/mg (potassium), 10123 ng/mg (calcium), 7836 ng/mg (chlorine), 3293 ng/mg (silicon), 2569 ng/mg (aluminum), 2102 ng/mg (sulfur), and 634 ng/mg (phosphorus) as presented in Table 1. In the case of micro-elements, iron had the highest concentration of 402 ng/mg followed by 91 ng/mg (scandium), 20 ng/mg (titanium), and 52 ng/mg (zinc) while Chromium, Manganese, Cobalt, and Copper had lower concentrations ranging from below 20 ng/mg. A trace amount of 27 ng/mg (Barium) was also observed which could be toxic to the growth of plants.

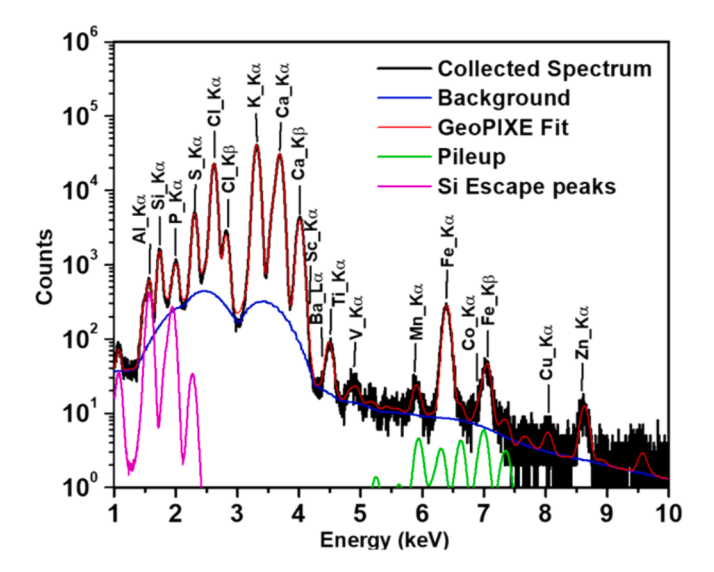


Fig. 2. Micro-PIXE Spectrum obtained from *Ocimum sanctum* (Tulsi) leaf over the scanned region of 375 \times 375 μm^2 .

Table 1
Elemental concentrations, uncertainties, and minimum detection limits (MDL) of different elements found in *Ocimum sanctum* (Tulsi) leaf as obtained using GeoPIXE.

Elements	Concentration (ng/mg)	Uncertainty (ng/mg)	MDL (ng/mg)
Al	2569	57	62
Si	3293	43	19
P	634	13	9.2
S	2102	11	5.5
Cl	7863	25	4
K	12633	33	3.1
Ca	10123	32	3
Sc	91	8	2.2
Ti	20	1	1.2
V	2.6	0.8	1.3
Mn	12	2	1.8
Fe	402	7	2.2
Co	8	2	2.6
Cu	9	2	4.7
Zn	52	3	5.3
Ba	27	4	5.3

The plant leaves have higher concentrations of K and Ca as observed in the current experiment because of their main function to perform ion transportation, enzyme activation, and absorption mechanisms in plants [33,34]. Cl, Si, and P help in stomatic functions, defense mechanisms and reduce abiotic stress to promote the growth of plants and are vital for fundamental biological processes, including carbohydrate metabolism, and diffusion and osmosis mechanisms [35,36,37]. Microelements like Fe, Zn, and Mn play an important role in cellular processes, enzymatic reactions, and photosynthetic processes [35,38]. However, the presence of barium could be from the soil used to grow the Tulsi plant. It is toxic and can disturb the nutritional intake of the plant [39,40].

Elemental concentrations were further investigated from the elemental maps using two types of correlation studies (Fig. 3) i.e., elemental and concentration phase correlations. Elemental correlation involves analyzing the concentrations and spatial relationships of elements within a specific ROI within the elemental maps. The concentration ratios are studied using correlation maps.

5.1.1. Elemental correlation analysis

The elemental distribution was also studied with the help of multielemental maps (Fig. 4). Iron was observed near the thinner area of the leaf while potassium, sulfur, calcium and chlorine seem to be distributed over the thicker areas. Multi-elemental map showcased the area where certain elements are present in the leaf which is used to estimate the function as well as the nutritional impact of those elements inside the leaf. To study the observed distributions quantitively, elemental correlation and phase correlation were used.

Elemental correlations were studied from the Fe map shown in Fig. 5 (a) and 5(b). The encircled ROI, being high-concentration regions, was analysed. It gives a comprehensive approach to examine the contribution of different elements in the selected region as shown in Table 2. It was observed that the concentrations of macro-elements like silicon and aluminum were highest whereas potassium, calcium, chlorine, sulphur were lower. Scandium, titanium and vanadium were the few of the micro-elements found in this region along with trace amounts of barium. Hence, this technique helps in comparing the concentrations of elements in different ROIs' along with uncertainties and MDL.

5.1.2. Phase correlation analysis

The (Fig. 6) correlation map between K and Ca illustrates the area on elemental maps where the encircled concentration ratio between the elements exists [41,42]. Ca to K concentration ratio was 1.8: 2.3 in weight percentage (wt%) which is equal to 10^4 ng/mg. This ROI was chosen to analyze the phase representing the lower concentration ratios

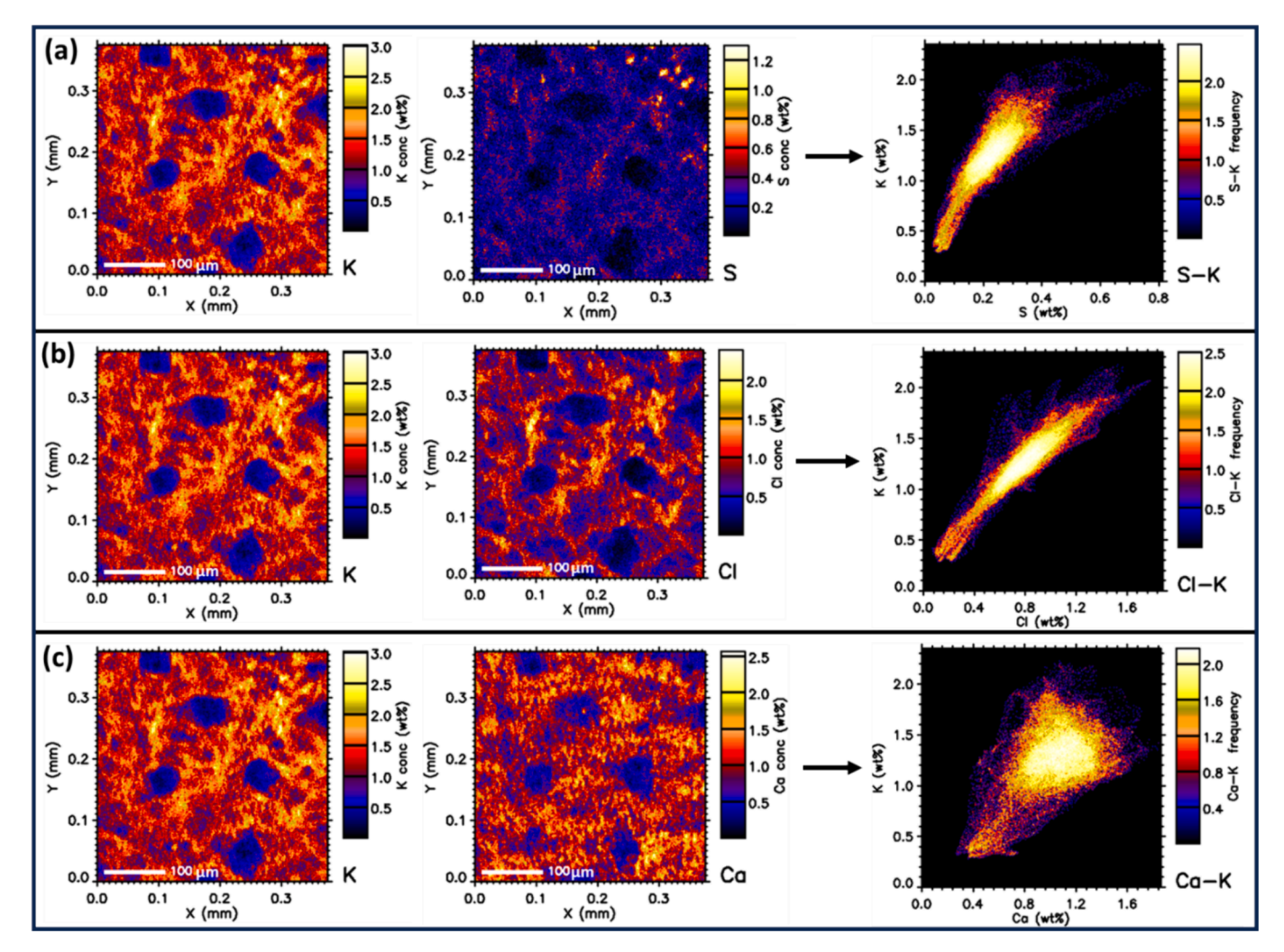


Fig. 3. Elemental maps (left) leading to correlation maps (right) obtained from potassium comparing with respect to (a) sulphur, (b) chlorine, and (c) calcium respectively.

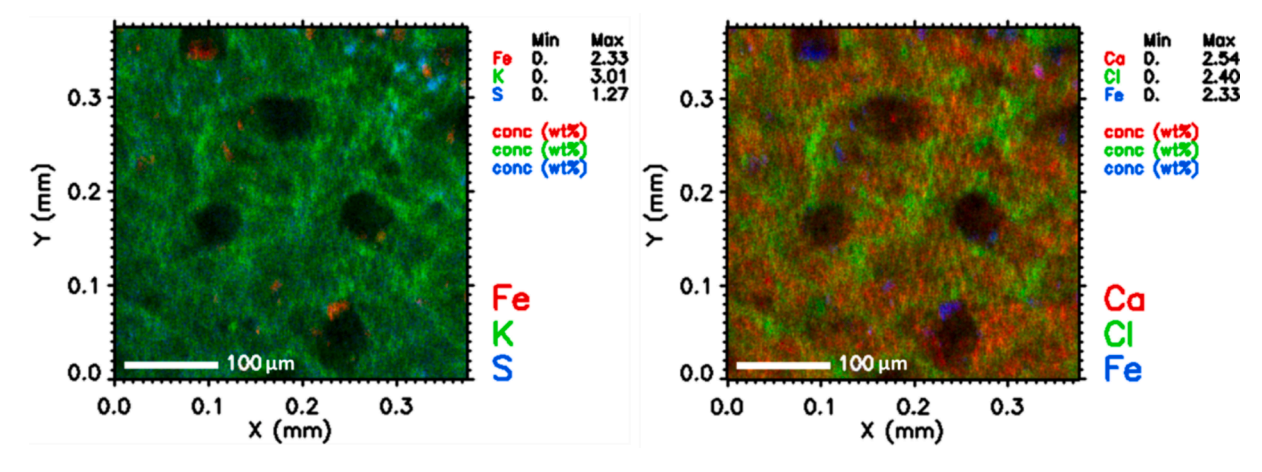


Fig. 4. Multi-Elemental maps of *Ocimum sanctum* (Tulsi) leaf. The blackened circular areas are the regions with lower concentration. The different colours in the map corresponds to different elements.

of both elements. Table 3 shows the elemental distribution of the selected region which mostly comprised of S, $\rm Cl$, K and $\rm Ca$.

Similarly, the difference was observed (Fig. 7a and Fig. 7b) in the sample's overall composition and ROI composition, which was expected.

The two distinct phases depicted in the correlation map align with varying concentration ratios of the elements. Fig. 7(a) corresponds to a lower concentration region of calcium in relation to potassium (with a concentration ratio of approximately (1.1:1). This ratio's distribution is evident in the elemental maps of calcium and potassium, revealing

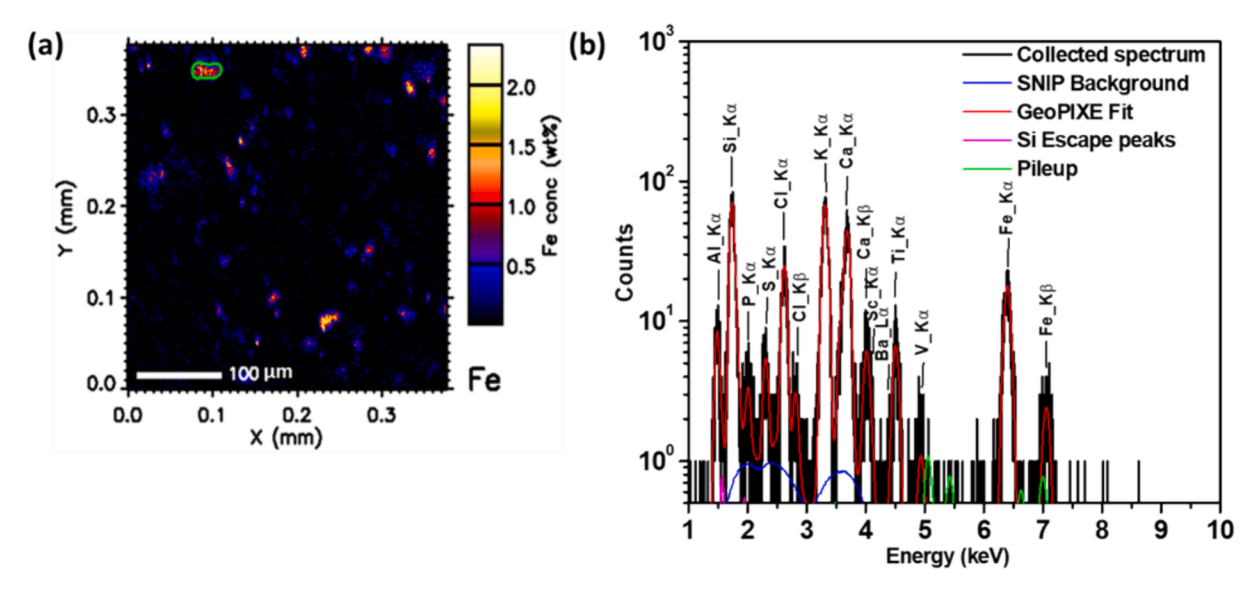


Fig. 5. (a) Iron map, and (b) PIXE spectrum obtained from the ROI taken within the iron map of an Ocimum sanctum (Tulsi) leaf.

Table 2Elemental concentration, uncertainty, and MDL extracted from the ROIs' within the iron map.

the non-map.					
Elements	Concentration (ng/mg)	Uncertainty (ng/mg)	MDL (ng/mg)		
Al	26268	2232	2071		
Si	48538	1683	424		
P	610	112	162		
S	596	65	79		
Cl	2377	90	58		
K	5981	126	51		
Ca	4077	128	53		
Sc	134	46	67		
Ti	969	84	79		
V	203	52	102		
Fe	7567	278	213		
Ba L	683	211	342		

thinner regions of the leaf. Conversely, Fig. 7(b) corresponds to a higher concentration region of calcium and potassium. The concentration ratio of calcium to potassium is approximately 4:5, which was from a relatively thicker areas of the leaf. Table 4 details the elemental distribution within these correlation element ratios. ROI in Fig. 7(a) exhibits a higher concentration of a few macro-elements and several micro-elements like Al, Si, Ti, Cu, Zn and Ba. The ROI in Fig. 7(b) shows higher concentrations of most macro- elements such as P, S, Cl, K and Ca, as well as some micro-elements like Sc, Mn, and Fe. Therefore, this technique gives information about the phases related to different concentration regions and the different elements composing them.

5.2. Broad-beam PIXE

Elemental concentrations obtained from broad-beam results were suspected to be contaminated with the graphite powder therefore separate scans on graphite powder were carried out. The obtained spectra from the graphite and leaf samples are shown in Fig. 8. Vanadium and iron were found to be the highest impurity elements. The contaminations were subtracted from the leaf sample concentrations.

The observed concentrations of elements followed the similar trend like in micro-PIXE (Table 5). Potassium (5788 ng/mg) and Calcium (5648 ng/mg) were higher than other macro-elements followed by Chlorine (2701 ng/mg), Silicon (1550 ng/mg), Aluminum (763 ng/mg) and Sulphur (653 ng/mg). Iron (80 ng/mg), Scandium (37 ng/mg) and Titanium (21 ng/mg) were higher in the category of micro-elements.

 $\begin{tabular}{ll} \textbf{Table 3} \\ Elemental concentration, uncertainty, and MDL extracted from the ROI in the K-Ca correlation map. \\ \end{tabular}$

Elements	Concentration (ng/mg)	Uncertainty (ng/mg)	MDL (ng/mg)
P	427	115	206
S	486	91	125
Cl	2189	128	92
K	3410	145	72
Ca	7027	202	68
Sc	119	51	49

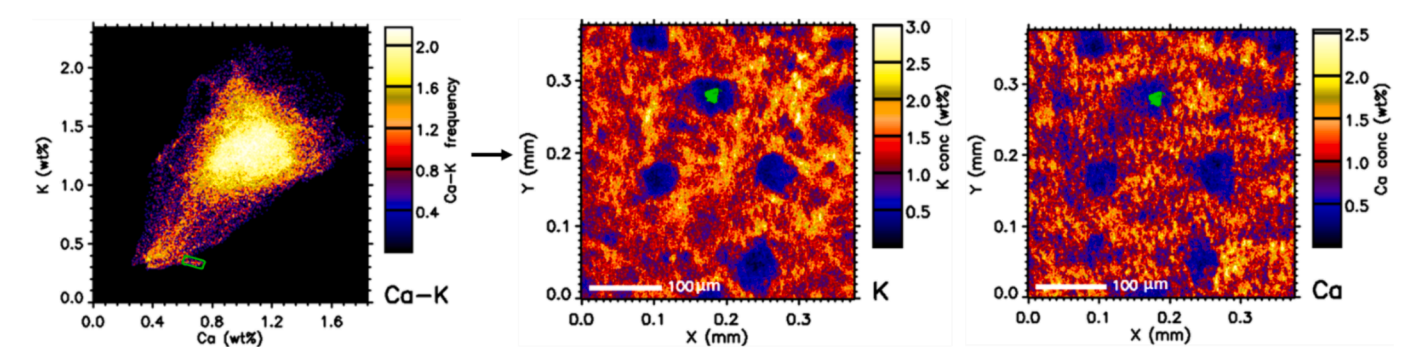


Fig. 6. ROI from the elemental correlation map of *Ocimum sanctum* (Tulsi) leaf showing the highlighted areas in the elemental maps corresponding to the marked concentration ratios of potassium and calcium.

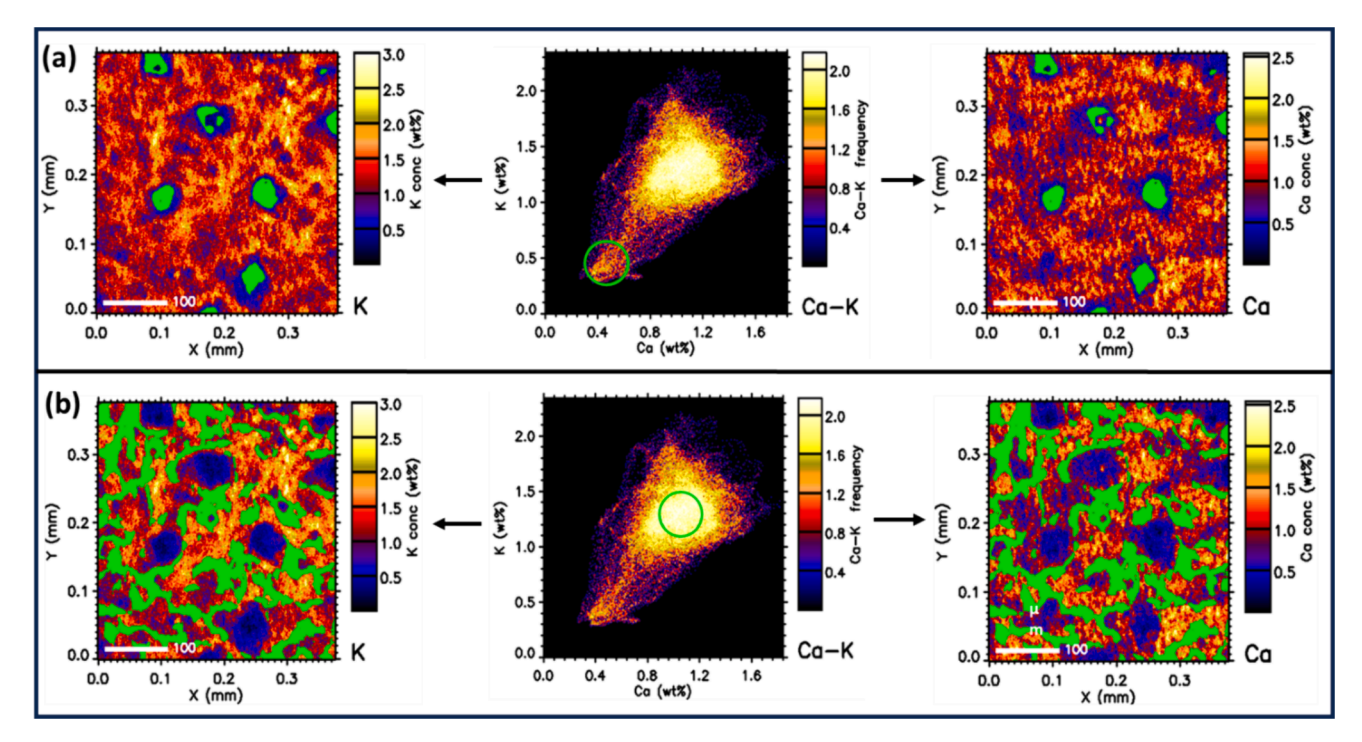


Fig. 7. Elemental correlation map from Ocimum sanctum (Tulsi) leaf from (a) low-concentration ratios and (b) higher concentration ratio representing the distribution of the elemental maps of Potassium and Calcium.

Table 4
Elemental concentration, uncertainty, and MDL extracted from the different ROI in the K-Ca correlation map.

Elements	ROI (a)			ROI (b)		
	Concentration (ng/mg)	Uncertainty (ng/mg)	MDL (ng/mg)	Concentration (ng/mg)	Uncertainty (ng/mg)	MDL (ng/mg)
Al	2911	248	321	2480	91	112
Si	6869	156	98	2465	35	34
P	380	27	49	666	13	17
S	415	19	30	2225	13	10
Cl	1857	27	22	8152	19	8
K	4020	36	17	13027	22	6
Ca	4432	37	16	10545	20	6
Sc	53	10	12	100	5	4
Ti	62	8	6	9	2	2
Mn	0	6	10	9	2	3
Fe	687	30	12	244	6	4
Cu	31	9	24	8	3	8
Zn	76	17	28	55	5	10
Ba	47	18	28	31	6	10

6. Conclusion

This study reports the elemental concentration and phase correlation between the macro and micro-elements found in Ocimum sanctum (Tulsi) leaf. In the micro-beam scans the concentrations of potassium (12633 ng/mg) and calcium (10123 ng/mg) were found to be in the highest range among the macro-elements. The concentrations of Iron (402 ng/ mg) and Scandium (91 ng/mg) were found to be in the highest range among the micro-elements. The PIXE runs using broad-beam revealed a similar concentration distribution pattern among the macro and microelements. Iron was observed near the thinner area of the leaf while potassium, sulfur, calcium and chlorine seem to be distributed over the thicker areas. In a region with higher iron concentration, it was observed that the concentrations of macro-elements like silicon and aluminum were highest whereas potassium, calcium, chlorine, sulphur were lower. Calcium and potassium concentrations were found to be well corelated. Their concentrations were higher in the thicker portion of the leaf as compared to the thinner region. The elemental concentration phasecorrelation techniques can be further used to study the relationship between various elements present at different parts of plants such as stem, root and flower section of the plant. The spectrum analysis from a specific ROI within an elemental map can give information about the dominating elements in that region which will help in understanding the nutrient flow in the leaves. Moreover, the change in concentration and spatial distribution of elements in different ROI helps in studying the role of each element in a particular area of the sample.

CRediT authorship contribution statement

Darshpreet Kaur Saini: Conceptualization, Experimentation, Data curation, Formal analysis, Writing – original draft, Writing – review & editing. **Todd A. Byers:** Experimentation, Data curation, Formal analysis, Writing – review & editing. **Cory Nook:** Experimentation, Data curation, Writing – review & editing. **Charles T. Bowen:** Experimentation, Data curation, Writing – review & editing. **Mohin Sharma:** Experimentation, Data curation, Writing – review & editing.

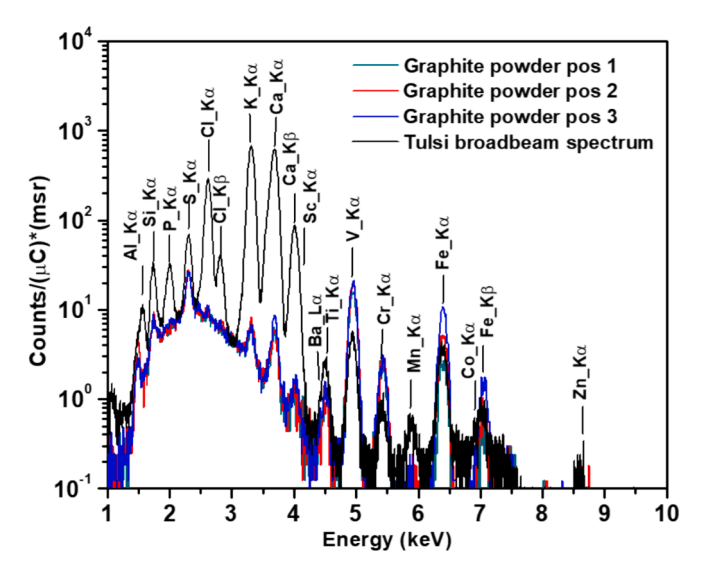


Fig. 8. Broad-beam PIXE Spectrum obtained from *Ocimum sanctum* (Tulsi) leaf over the scanned region. The colored spectra were extracted from different regions on graphite powder pellets.

Table 5Elemental concentrations, uncertainties, and minimum detection limits of elements obtained in *Ocimum sanctum* (Tulsi) leaf from broad-beam PIXE analysis.

Elements	Concentration (ng/mg)	Uncertainty (ng/mg)	MDL (ng/mg)
Al	763.3903	29.9145	40.9402
Si	1550.071	20.5128	12.7350
P	508.6752	8.7179	7.6068
S	653.2764	5.3846	4.4444
Cl	2700.812	10.1709	3.1624
K	5787.821	14.4444	2.3932
Ca	5648.59	13.0769	2.1367
Sc	37.4359	2.3077	1.5385
Ti	21.8091	0.9402	0.7692
V	1.95156	1.2821	0.7949
Mn	7.3504	0.7692	1.11111
Fe	80.285	2.5641	1.4530
Co	7.0940	1.2821	1.6239
Zn	12.820	1.6239	2.9060
Ba L	12.051	2.7350	3.5043

Mritunjaya Parashar: Experimentation, Data curation, Writing – review & editing. **Gary A. Glass:** Supervision, Funding acquisition, Resources, Writing – review & editing. **Bibhudutta Rout:** Conceptualization, Funding acquisition, Project administration, Resources, Supervision, Writing – original draft, Writing – review & editing.

Declaration of competing interest

The authors declare that they have no known competing financial interests or personal relationships that could have appeared to influence the work reported in this paper.

Data availability.

All the data generated or analyzed during this study are included in the published article. Any data related to this study and its supplementary information can be provided with a reasonable request.

Acknowledgments

We acknowledge partial support from NIH grant #NIH-R01DK109382 and NSF grants #HBCU-EiR-2101181 and ECCS-

2210722.

Appendix A. Supplementary data

SI includes the expanded spectrum obtained from micro-PIXE and generated in GeoPIXE. It shows the DA fit to each element lying within energy range of 3 keV to 6 keV. This helps in differentiating the contribution of characteristic X-rays originating from transitions of electrons from different shells, such as K_{α} and K_{β} . Supplementary data to this article can be found online at https://doi.org/10.1016/j.nimb.20 24.165412.

References

- A. Parveen et al., "Tulsi," Essentials of Medicinal and Aromatic Crops, pp. 983–1008, 2023, doi: 10.1007/978-3-031-35403-8_38.
- [2] F. Bilo, et al., Elemental analysis of tree leaves by total reflection X-ray fluorescence: New approaches for air quality monitoring, Chemosphere 178 (Jul. 2017) 504–512, https://doi.org/10.1016/J.CHEMOSPHERE.2017.03.090.
- [3] S. Singh, et al., Investigation on major, minor and trace elements in some medicinal plants using Particle Induced X-ray Emission, J. Radioanal. Nucl. Chem. 323 (3) (Mar. 2020) 1443–1449, https://doi.org/10.1007/S10967-020-07032-9/ METRICS
- [4] R. Gowrishankar, et al., Trace element studies on tinospora cordifolia (Menispermaceae), Ocimum sanctum (Lamiaceae), moringa oleifera (Moringaceae), and phyllanthus niruri (Euphorbiaceae) using PIXE, Biol. Trace Elem. Res. 133 (3) (Mar. 2010) 357–363, https://doi.org/10.1007/S12011-009-8439-1/TABLES/3.
- [5] C.A. Gunawardana, et al., Magnesium stearate surface coverage on tablets and drug crystals: Insights from SEM-EDS elemental mapping, Int. J. Pharm. 630 (Jan. 2023) 122422, https://doi.org/10.1016/J.IJPHARM.2022.122422.
- [6] T. Wirtz, P. Philipp, J.N. Audinot, D. Dowsett, S. Eswara, High-resolution high-sensitivity elemental imaging by secondary ion mass spectrometry: from traditional 2D and 3D imaging to correlative microscopy, Nanotechnology 26 (43) (Oct. 2015) 434001, https://doi.org/10.1088/0957-4484/26/43/434001.
- [7] V. Lazic, M. Vadrucci, R. Fantoni, M. Chiari, A. Mazzinghi, A. Gorghinian, Applications of laser-induced breakdown spectroscopy for cultural heritage: A comparison with X-ray Fluorescence and Particle Induced X-ray Emission techniques, Spectrochim. Acta Part B At. Spectrosc. 149 (Nov. 2018) 1–14, https:// doi.org/10.1016/J.SAB.2018.07.012.
- [8] S. Bernard, K. Benzerara, O. Beyssac, G.E. Brown, L.G. Stamm, P. Duringer, Ultrastructural and chemical study of modern and fossil sporoderms by Scanning Transmission X-ray Microscopy (STXM), Rev. Palaeobot. Palynol. 156 (1–2) (Jul. 2009) 248–261, https://doi.org/10.1016/J.REVPALBO.2008.09.002.
- [9] G.A. Glass, A.D. Dymnikov, B. Rout, J.F. Dias, L.M. Houston, J. Leblanc, Magnetic quadrupole doublet focusing system for high energy ions, Rev. Sci. Instrum. 79 (3) (Mar. 2008) 36102, https://doi.org/10.1063/1.2890101/350759.
- [10] S. A. E. Johansson, J. L. Campbell, and K. G. Malmqvist, "Particle-induced X-ray emission spectrometry (PIXE)," p. 451, 1995, Accessed: Feb. 03, 2024. [Online]. Available: https://www.wiley.com/en-us/Particle+Induced+X+Ray+Emission+Spectrometry+%28PIXE%29-p-9780471589440.
- [11] E.F. Garman, G.W. Grime, Elemental analysis of proteins by microPIXE, Prog. Biophys. Mol. Biol. 89 (2) (Oct. 2005) 173–205, https://doi.org/10.1016/J. PBIOMOLBIO 2004 09 005
- [12] E. Bakkaus, et al., Concentration and distribution of cobalt in higher plants: The use of micro-PIXE spectroscopy, Nucl. Instrum. Meth. Phys. Res. B 231 (1–4) (Apr. 2005) 350–356, https://doi.org/10.1016/J.NIMB.2005.01.082.
- [13] G.J. Naga Raju, et al., Estimation of trace elements in some anti-diabetic medicinal plants using PIXE technique, Appl. Radiat. Isot. 64 (8) (Aug. 2006) 893–900, https://doi.org/10.1016/J.APRADISO.2006.02.085.
- [14] J. Mesjasz-Przybylowicz, W.J. Przybylowicz, Micro-PIXE in plant sciences: Present status and perspectives, Nucl. Instrum. Methods Phys. Res. B 189 (1–4) (Apr. 2002) 470–481, https://doi.org/10.1016/S0168-583X(01)01127-2.
- [15] T.A. Byers, J.E. Manuel, A.G. Ponette-Gonzalez, T.E. Gill, G.A. Glass, Analysis of rain-deposited dust on polysulfone membranes using proton-induced X-ray emission spectroscopy, Microchem. J. 192 (Sep. 2023) 108928, https://doi.org/ 10.1016/J.MICROC.2023.108928.
- [16] C.A. Pineda-Vargas, M.E.M. Eisa, A.L. Rodgers, Characterization of human kidney stones using micro-PIXE and RBS: A comparative study between two different populations, Appl. Radiat. Isot. 67 (3) (Mar. 2009) 464–469, https://doi.org/ 10.1016/J.APRADISO.2008.06.036.
- [17] A. Re, et al., Lapis lazuli provenance study by means of micro-PIXE, Nucl. Instrum. Meth. Phys. Res. B 269 (20) (Oct. 2011) 2373–2377, https://doi.org/10.1016/J. NIMB 2011 02 070
- [18] H. Sadek, µ-PIXE mapping of archeological glazed pottery from Egypt, Appl. Surf. Sci. 332 (Mar. 2015) 281–286, https://doi.org/10.1016/J.APSUSC.2015.01.115.
- [19] Q.Q. Wu, et al., PIXE-RBS analysis on potteries unearthed from Lijiaba Site, Nucl. Instrum. Meth. Phys. Res. B 296 (Feb. 2013) 1–6, https://doi.org/10.1016/J. NIMB 2012 12 004
- [20] O. Kakuee, V. Fathollahi, P. Oliaiy, M. Lamehi-Rachti, R. Taheri, H.A. Jafarian, External PIXE analysis of an Iranian 15th century poetry book, Nucl. Instrum. Methods Phys. Re.s B 273 (Feb. 2012) 178–181, https://doi.org/10.1016/J. NIMB.2011.07.069.

- [21] P. Joshi, D. Mehta, Effect of dehydration on the nutritive value of drumstick leaves, J. Metabolomics Syst. Biol. 1 (1) (Aug. 2010) 5–9, https://doi.org/10.5897/ JMSB.900003.
- [22] S.R. Navale, U. Supriya, V.M. Harpale, K.C. Mohite, Effect of Solar Drying on the Nutritive Value of Fenugreek Leaves, Int. J. Eng. Adv. Technol. (IJEAT) 2 (2014) 2249–8958.
- [23] B. Mohanta, A. Chakraborty, M. Sudarshan, R. K. Dutta, and M. Baruah, "Elemental profile in some common medicinal plants of India. Its correlation with traditional therapeutic usage," J. Radioanal. Nucl. Chem. 2003 258:1, vol. 258, no. 1, pp. 175–179, Oct. 2003, doi: 10.1023/A:1026291000167.
- [24] F.D. McDaniel, J.L. Duggan, C. Yang, B.N. Guo, M. El Bouanani, M. Nigam, The high-energy heavy ion nuclear microprobe at the University of North Texas, Nucl. Instrum. Methods Phys. Res. B 181 (1–4) (Jul. 2001) 99–103, https://doi.org/ 10.1016/S0168-583X(01)00567-5.
- [25] B. Rout, et al., An overview of the facilities, activities, and developments at the University of North Texas Ion Beam Modification and Analysis Laboratory (IBMAL), AIP Conf. Proc. 1544 (1) (Jul. 2013) 11–18, https://doi.org/10.1063/ 1.4813454
- [26] M. Parashar, et al., Probing elemental diffusion and radiation tolerance of perovskite solar cells via non-destructive Rutherford backscattering spectrometry, APL Energy 2 (1) (Mar. 2024) 16109, https://doi.org/10.1063/5.0193601.
- [27] X-123SDD Complete X-Ray Spectrometer with Silicon Drift Detector (SDD) Amptek – X-Ray Detectors and Electronics." Accessed: Aug. 03, 2022. [Online]. Available: https://www.amptek.com/internal-products/obsolete-products/sdd-x-ray-detectors-for-xrf/x-123sdd-complete-x-ray-spectrometer-with-silicon-drift-detectors-sdd
- [28] "Oxford Microbeams Ltd." Accessed: Jan. 04, 2024. [Online]. Available: http://www.microbeams.co.uk/.
- [29] C.G. Ryan, Quantitative trace element imaging using PIXE and the nuclear microprobe, Int. J. Imaging Syst. Technol. 11 (4) (Jan. 2000) 219–230, https://doi. org/10.1002/JMA.1007
- [30] C.G. Ryan, D.N. Jamieson, C.L. Churms, J.V. Pilcher, A new method for on-line true-elemental imaging using PIXE and the proton microprobe, Nucl. Instrum. Methods Phys. Res. B 104 (1–4) (Sep. 1995) 157–165, https://doi.org/10.1016/ 0168-583X(95)00404-1.
- [31] C.G. Ryan, D.N. Jamieson, Dynamic analysis: on-line quantitative PIXE microanalysis and its use in overlap-resolved elemental mapping, Nucl. Instrum.

- Methods Phys. Re.s B 77 (1-4) (May 1993) 203-214, https://doi.org/10.1016/0168-583X(93)95545-G.
- [32] K. Vogel-Mikuš, et al., Spatial distribution of cadmium in leaves of metal hyperaccumulating Thlaspi praecox using micro-PIXE, New Phytol. 179 (3) (Aug. 2008) 712–721, https://doi.org/10.1111/J.1469-8137.2008.02519.X.
- [33] E. Epstein, The essential role of calcium in selective cation transport by plant cells, Plant Physiol. 36 (4) (Jul. 1961) 437, https://doi.org/10.1104/PP.36.4.437.
- [34] H J Evans and G. J. Sorger, "Role of Mineral Elements with Emphasis on the Univalent Cations," https://doi.org/10.1146/annurev.pp.17.060166.000403, vol. 17, no. 1, pp. 47–76, Nov. 2003, doi: 10.1146/ANNUREV.PP.17.060166.000403.
- [35] G. C. M. Teixeira, R. de Mello Prado, K. S. Oliveira, V. D'Amico-Damião, and G. da Silveira Sousa Junior, "Silicon Increases Leaf Chlorophyll Content and Iron Nutritional Efficiency and Reduces Iron Deficiency in Sorghum Plants," J Soil Sci Plant Nutr, vol. 20, no. 3, pp. 1311–1320, Sep. 2020, doi: 10.1007/S42729-020-00214-0/FIGURES/14.
- [36] M. Razaq, P. Zhang, H.L. Shen, Salahuddin, Influence of nitrogen and phosphorous on the growth and root morphology of Acer mono, PLoS One 12 (2) (Feb. 2017) e0171321.
- [37] H. Marschner, "Mineral Nutrition of Higher Plants 2nd Edition," p. 889, 1955.
- [38] M. Hasani, Z. Zamani, G. Savaghebi, R. Fatahi, Effects of zinc and manganese as foliar spray on pomegranate yield, fruit quality and leaf minerals, J. Soil Sci. Plant Nutr. 12 (3) (2012) 471–480, https://doi.org/10.4067/S0718-95162012005000009
- [39] R. Suwa, K. Jayachandran, N.T. Nguyen, A. Boulenouar, K. Fujita, H. Saneoka, Barium toxicity effects in soybean plants, Arch. Environ. Contam. Toxicol. 55 (3) (Oct. 2008) 397–403, https://doi.org/10.1007/S00244-008-9132-7/TABLES/3.
- [40] M. Llugany, C. Poschenrieder, J. Barceló, Assessment of barium toxicity in bush beans, Arch. Environ. Contam. Toxicol. 39 (4) (Feb. 2000) 440–444, https://doi. org/10.1007/S002440010125/METRICS.
- [41] B. Rout, J. Hendriks, D.N. Jamieson, R. Szymanski, D. Milliken, S.X. Dou, Nuclear microprobe analysis of U-doped (Bi, Pb)2Sr2Ca2Cu3Oy/Ag superconducting tapes, Nucl. Instrum. Methods Phys. Res. B 190 (1–4) (May 2002) 357–364, https://doi. org/10.1016/S0168-583X(01)01318-0.
- [42] B. Rout, D.N. Jamieson, T. Hopf, C.G. Ryan, Phase correlations of elemental maps using nuclear microscopy, Nucl. Instrum. Methods Phys. Res. B 210 (Sep. 2003) 129–134, https://doi.org/10.1016/S0168-583X(03)01082-6.